SUNFLOWER

"Sustainable Novel Flexible Organic Watts Efficiently Reliable"

Grant agreement No.: 287594 (Integrated Project)

Deliverable 2.3: Nanoscale 3D imaging of active layers and interfaces in the most promising device architectures

Due date of deliverable: 30 September 2014
Actual submission date: 22 Septermber 2014

Start date of project: 1st October 2011   Duration: 48 months

Coordinator	CSEM
Deliverable Leading Partner	UA
Contributing Partners	UJI, CSEM, CNR, CNRS
Task	
Revision	UJI (A. Guerrero), CSEM (T. Offermans), CNR (M. Seri)

Project co-funded by the European Commission under the Seventh Framework Programme (FP7)		
Dissemination Level		
PU	Public	X
PP	Restricted to other programme participants (including the Commission Services)	
RE	Restricted to a group specified by the consortium (including the Commission Services)	
CO	Confidential, only for members of the consortium (including the Commission Services)	

Table of Contents

List of figures and Tables

Abbreviations

TEM	Transmission Electron Microscopy
STEM	Scanning Transmission Electron Microscopy
FIB	Focused Ion Beam
SEM	Scanning Electron Microscope
HAADF	High Angle Annular Dark Field imaging
EELS	Electron Energy Loss Spectroscopy
SIRT	Simultaneous Iterative Reconstruction Technique
STEMSI	Scanning Transmission Electron Microscopy Spectral Imaging
ITO	Indium Tin Oxide
PCBM	Phenyl-C61-Butyric acid Methyl ester
P3HT	Poly-3-Hexyl Thiophene
ODCB	Ortho-DiChloroBenzene
PEDOT:PSS	Poly(3,4-Ethylene DiOxy Thiophene) PolyStyrene Sulfonate
PDPP5T	PolyDiketo Pyrrolo Pyrrole-Quintet Thiophene
BHJ	Bulk HeteroJunction
PSD	Power Spectral Density

1 Introduction

1.1 Purpose of this plan/ report

The purpose of this report is to demonstrate the ability to characterize the morphology of the active layers in three dimensions by electron tomography. This achievement goes beyond the state-of-the-art and has been enabled through advanced, aberration corrected electron microscopy. This deliverable will play a major role during the remainder of the project.

1.2 Description of the deliverable

Nanoscale 3D imaging of active layers and interfaces in the most promising device architectures: This study will allow the investigation of complex multi-layered systems in which hard and soft materials (polymers) are combined in OPV devices. 3D organization of the photoactive layer and the various interfaces in the device structure, that depend on the materials combination and the chosen processing route, will be investigated and described. Such information will be linked to complementary analytical data (D2.5) to correlate morphological, optical, and electrical properties of the devices.

1.3 Related deliverables and milestones

INPUT:

D1.9	Optimal High and low bandgap polymer solution
D2.2	Tandem cells with 7% efficiency, using most promising architecture and materials

OUTPUT:

-	Most promising devices
D2.9	(hero) Cells with 10% efficiency (tandem or ternary blends SJ) by simultaneous optimization of light in-coupling, light management, charge transport and current collection.

2   Methodology

2.1   Electron tomography

Conventional transmission electron microscopy (TEM) only provides a two-dimensional (2D) projection of a three-dimensional (3D) object, which prohibits a quantitative interpretation of any materials structure. This problem can be overcome by using electron tomography. Electron tomography is a technique in which the internal 3D structure of a structure is reconstructed from a series of 2D projection images acquired using a TEM. The 2D projections for materials science samples can be obtained using a high angle annular dark field detector in scanning transmission electron microscopy mode (HAADF-STEM) [1]. The sequence of projections, the so called the 'tilt series', is acquired over a large range of tilt (usually ±70°) with increments of typically 2° (Figure 1). The tilt series is then aligned with regard to a common tilt axis and used as an input for a 3D reconstruction algorithm. A 3D reconstruction can be made using a variety of mathematical algorithms but the most common ones are iterative techniques in which the initial reconstruction is refined iteratively [1].
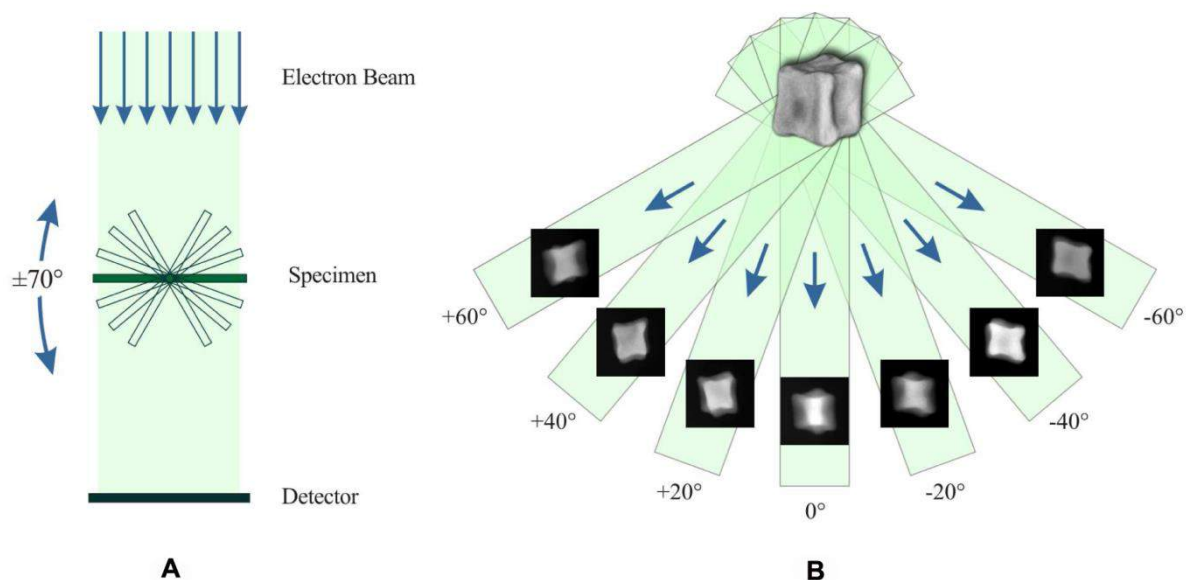
Figure 1: (A), An overview of the electron tomography experiment; the specimen is tilted over a wide tilt range at small angular increments and at each tilt a projection electron image is acquired at the detector. (B) A series of projections which are acquired for an Au nanoparticle over the tilt range of ±60° using HAADF detector is shown. These images are later used as input for computed tomography algorithm in order to reconstruct the 3D internal structure of the nanoparticle.

2.2   Quantitative electron tomography

Although electron tomography has been successfully applied on many nanostructures results are merely qualitative. This is related to a number of inherent artefacts connected to the technique itself. For example, in an electron microscope it is often impossible to tilt the samples over ±90°, due to the limited spacing in between the pole pieces of the objective lens of the microscope leading to a lack of projections for a range of angles, the so called 'the missing wedge'. The missing wedge is the main source of elongation artefact along one tomography axis (electron optical axis) which leads to anisotropy of resolution in the final 3D reconstruction [2]. The missing wedge as a major electron tomography artefact hampers a correct quantification of the 3D reconstruction. However in recent years this has been overcome by using a dedicated on-axis tomography holder which is able to rotate 360° in the

gap of the pole pieces of the objective lens, it is hereby possible to acquire projections of the object over ±90° tilt range. This method requires a micropillar sample which can be prepared using a DualBeam SEM/FIB machine. The procedure to prepare this micropillar is explained more extensively in section 2.3.

2.3   Optimization of sample preparation of pillar-shaped specimen

Standard preparation techniques such as ultra-microtomy and ion beam etching for TEM sample preparation are not able to provide cross-section TEM samples or micropillar specimens of complex multilayered systems in which hard and soft materials are combined. The only tool that overcomes this bottleneck and is able to prepare samples for such systems is focused ion beam (FIB). FIB uses heavy Ga^+ ions to mill away the materials from the specimen from several micrometers to nanometers. More advanced versions of FIB equipment integrate an electron column which is tuned at 52° with regard to the ion column in the so called DualBeam. This instrument provides SEM imaging of the nanomaterials while milling using Ga^+ ions.

The procedure of preparation of micropillar specimen is schematically summarized in Figure 2. A standard ion column allows Ga^+ milling at 5–30 kV. At first a layer of Pt is deposited (using ion-beam induced deposition) on the top of the specimen in order to provide a protective layer against the Ga^+ ion damage, which is illustrated in Figure 2A,B. Then using the ion beam, the specimen can be milled down to a slab type cross-section specimen or a micropillar with a diameter down to almost 100 nm (see Figure 2F). The micropillar is subsequently removed from the substrate and is welded on a special rod-shaped support. The support is mounted in an on-axis rotation tomography holder. Using this mechanism a rotation of 360° of the pillar-shaped specimen is possible inside the pole piece gap of a TEM.

One of the major challenges during preparation of a pillar-shaped specimen is to avoid or reduce the ion damage to the outer parts of the pillar. Using low voltage milling the damage can be reduced but one needs to take this into account specifically for beam sensitive materials while preparing the micropillar specimens.

Especially for soft materials, FIB preparation is far from straightforward. The procedure was therefore optimized for the samples investigated in this project. In this manner , a protocol has been developed in which the initial rough milling is carried out at high voltages and at high currents. This initial approach is followed by sequential steps at lower voltages and currents. The final milling steps, resulting in lamellae with a thickness of approximately of 80 nm or less are carried out at an acceleration voltage as low as 1 kV and a beam current of 75 pA. Using this approach a broad range of samples has been prepared with great success including polymers, porous membranes and biological cell tissue. Also needle shaped samples for electron tomography can nowadays be prepared successfully.
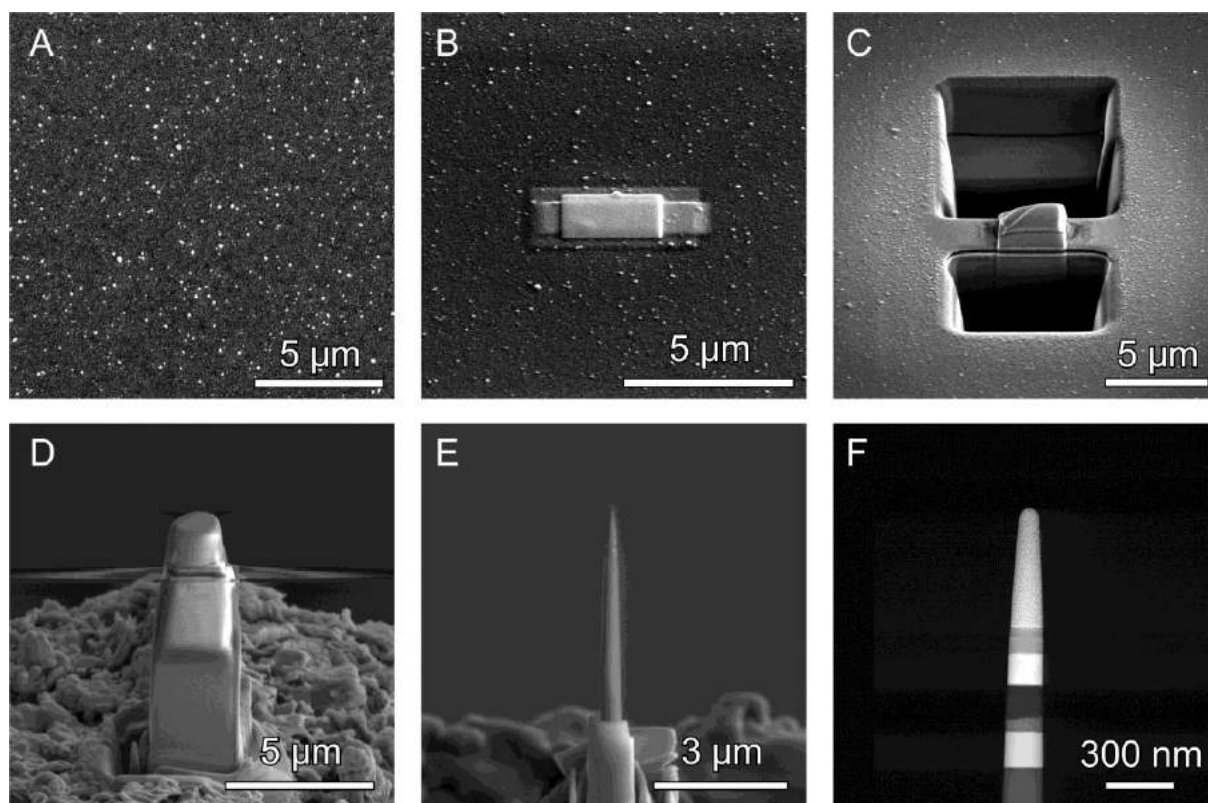
Figure 2: (A) The surface area of the sample from which the pillar-shaped samples is prepared. (B) A thin layer of Pt is deposited using e-beam deposition followed by another layer of thicker Pt deposited using ion-beam deposition. The role of deposited Pt is to protect the upper layer of the sample during milling using high energy Ga$^+$ ions. (C) Trenches are cut around the area of interest in order to perform a lift-out. (D,E) The area of interest is welded on top of a needle-shaped holder and is milled down to approximately 150 nm thickness. (F) HAADF-STEM image of the electron transparent pillar.

2.4   Optimization of electron tomography experiment

The Radon theory explains the fundamental relationship between an object and its lower dimensional projections. The work of Radon has been the basis for tomographic reconstruction, in which an object of higher dimension is reconstructed via a series of projections from lower dimensions. In electron tomography the same principles apply as long as the projection requirement for tomographic reconstruction is fulfilled [3]. Among all the imaging techniques in transmission electron microscopy, HAADF-STEM imaging is one of the few that satisfies the projection requirement even for crystalline materials since contrast is not based on diffraction. In HAADF-STEM imaging mode the intensity in the image is proportional to a projection (along the beam direction) of the atomic weight of the element raised to a power of approximately 2. Therefore the contrast in the image is based on the chemical composition of the specimen. The same principle is applied for electron energy-loss spectroscopy (EELS) under well-defined conditions [4]. This is why mostly these two imaging modes have been used throughout this report to provide structural as well as chemical three dimensional information of the device architecture.

Simultaneous iterative reconstruction technique (SIRT) is one of the most widely used reconstruction techniques for materials science samples. The technique refines the reconstructions iteratively to yield a more accurate reconstruction of the object. The iteration loop usually stops when convergence is achieved. Advanced reconstruction techniques such as total variation minimization (TVM), expectation maximization (EM) or discrete algebraic reconstruction technique (DART) are able to reconstruct the object using prior knowledge and therefore yield even more accurate 3D reconstruction of nanostructures. These techniques are calculation intensive and demand a more advanced knowledge about the mathematical principles of the technique.

2.5   3D imaging of photoactive layers

Whereas HAADF allows straightforward investigation of interfaces containing inorganic layers after successful sample preparation, contrast between different material domains within photoactive bulk heterojunction (BHJ) layers has been more challenging. Simultaneously a resolution of at least a few nanometers is required. TEM has been shown to be able to satisfy both requisites using analytical TEM modalities [5]. Here electron optical spectrometers are used to separate electrons that have passed the sample according to their suffered energy-loss after inelastic scattering. It was shown before that low energy-loss spectra with information around optical excitations can be used to distinguish different phases, i.e. polymer-enriched, fullerene-enriched as well as mixed phases [6]. Different carbonaceous materials show different excitations of valence electrons, which can either be band-gap, surface plasmon or bulk plasmon excitations. Irradiation with electrons causes rapid damage of organic materials. Hence, the electronic structure determining the band-gap is difficult to probe on the local scale. However, bulk plasmon excitations between ~20-25 eV are more stable since structures of damaging products of polymer chains and fullerene molecules are still different and can hence be distinguished [7]. We apply STEM in combination with EELS to visualize the morphology of photoactive layers in cross-sections and pillar-shaped samples prepared using FIB. This combination is called STEM spectral imaging (STEMSI) and offers spatially resolved low energy-loss spectroscopy at the nanoscale. After fitting, for example, a Gaussian profile to each spectrum, the determined mean positions can be mapped out. Resulting maps indicate plasmon peak positions, which differ depending on the localized enrichment of a certain material or on the amount of intermixing.

2.6   Application to the most promising device architectures

We first show for model device architectures that visualization of the device structure and nanoscale morphology of BHJ layers enables correlation of structure and processing parameters. Therefore the methodology is also applied to the most promising architecture, which is a tandem cell containing the following layers from bottom to top:

Indium tin oxide (ITO) / PEDOT:PSS (Al4083) / HBG-1:[60]PCBM / Zinc oxide (ZnO F29) / PEDOT:PSS (NT5-3435695-3) / PDPP5T:[60]PCBM / Calcium (Ca) / Aluminium (Al)

FIB-prepared, ultrathin cross-sections and micropillar samples are prepared for the fresh device and for the device after heating at 70° C for 2 min. Micropillar samples are further used for HAADF-STEM tomography of the recombination layer (ZnO / PEDOT:PSS). The pillar for the heated device is also used for STEMSI tomography. Here, not the HAADF signal is used for 3D reconstruction but the low energy-loss channels. Subsequently, plasmon peak fitting is extended to the reconstructed volume.

3 Results

3.1 Soft and hard matter interfaces

It is essential to determine the integrity of device layers at nanometer level after fabrication. There are very few characterization techniques that provide such information in 3D. Electron tomography as a powerful imaging technique has been used to characterize the interfaces of the model device (P3HT:PCBM) as well as the tandem cell. Figure 3A shows a projection image from an ultrathin, FIB-prepared, cross-section specimen. Note that the intensity in the image scales with the atomic number of the elements present in the sample. Almost no contrast is observed within the photoactive layers. Figure 3B on the other hand shows an orthogonal slice through the 3D reconstruction of the fresh device. This result was obtained using the procedure explained in section 2.1. The image indicates that numerous porosities are present in the Ca layer which can act as crack propagation sources if the device is exposed to mechanical forces. Although the reconstruction is qualitative in case of a slab-type specimen, it provides a large field of view for estimating the quality of interfaces. Figure 4 shows similar images of the device annealed for 2 min at 70° C. The interface structural changes upon annealing are insignificant. The PEDOT:PSS, which forms recombination layers with ZnO is not visible in the shown dark-field images but it will be revealed by 2D and 3D STEMSI analyses in sections 3.3 and 3.5.
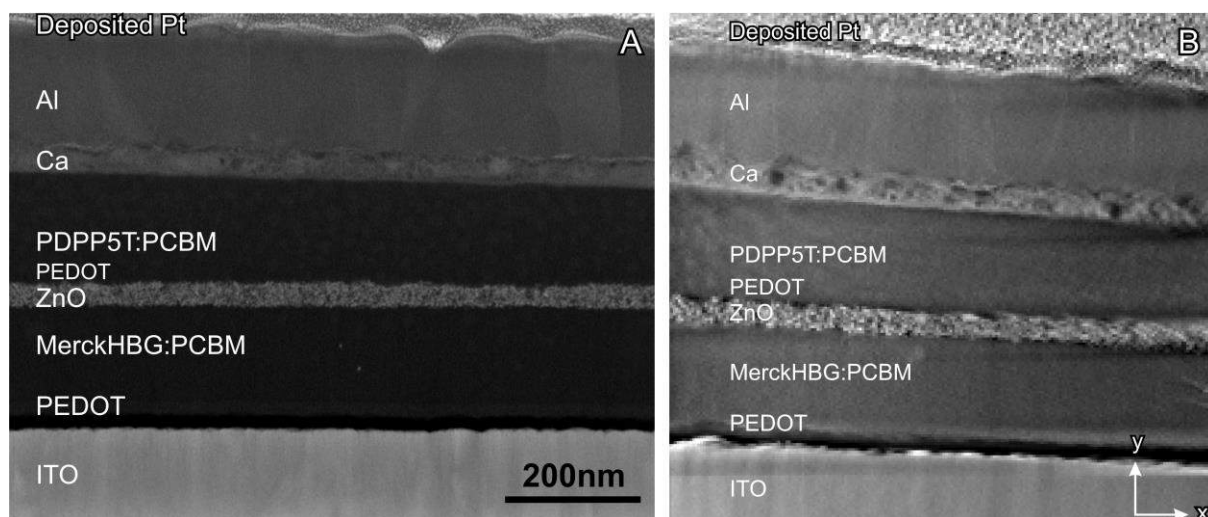
**Figure 3:** (A): HAADF-STEM projection image of a thin cross-section specimen made from a fresh tandem cell. (B) An orthosclice through the 3D reconstruction of the cross-section specimen.


Figure 4: (A) HAADF-STEM projection image of a thin cross-section specimen made from the annealed tandem cell (2 min at 70° C). (B) An orthoslice through the 3D reconstruction of the cross-section specimen.

The hard/soft matter interfaces between ZnO as the hole-blocking layer within the recombination layer and the organic layers in a tandem cell play an important role in the efficiency of the device. It is therefore crucial to investigate the porosity of this layer apart from its integrity. For this reason, two micropillar specimens are prepared for on-axis electron tomography experiments in order to perform a study of this layer in 3D. Figure 5A shows a projection image of the ZnO layer from the fresh tandem cell device. Clearly the HAADF-STEM imaging mode is unable to show any contrast in the organic photoactive layers, therefore we used STEMSI as explained in section 3.5 to perform nanoscale investigation on the organic blends. Using SIRT reconstruction technique, a 3D reconstruction of the ZnO layer is performed. In Figure 5B an orthoslice through the reconstruction is indicated, showing the porosity of the layer. Figure 5C is a volume rendering of the ZnO layer. The 3D reconstruction of the ZnO layer shows the roughness of the interface between the ZnO and the organic materials indicating that the area for charge extraction and recombination is much larger than the plane cross-sectional surface area.
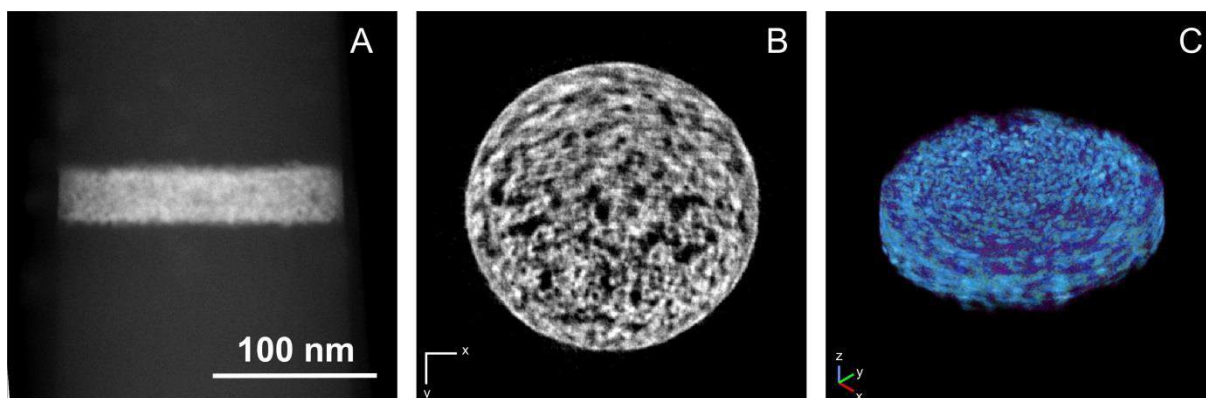
Figure 5: (A) HAADF-STEM projection image of the ZnO/organic interfaces for the fresh tandem cell. (B) An orthoslice through the 3D reconstruction of the ZnO layer in the micropillar specimen shows a porous ZnO structure. (C): Volume rendering image from the 3D reconstruction of the ZnO layer.

Figure 6A shows an HAADF-STEM projection image of the interface between the ZnO and organic layers for the annealed tandem cell device. For such a structure even qualitative comparison between Figure 5A and Figure 6A is not feasible. Comparing Figure 5B and Figure 6B shows that there are indeed very few structural changes taking place at the ZnO layer upon annealing. It will be investigated in section 3.5 using EELS-tomography whether the organic materials have penetrated into the pores of the ZnO upon deposition.
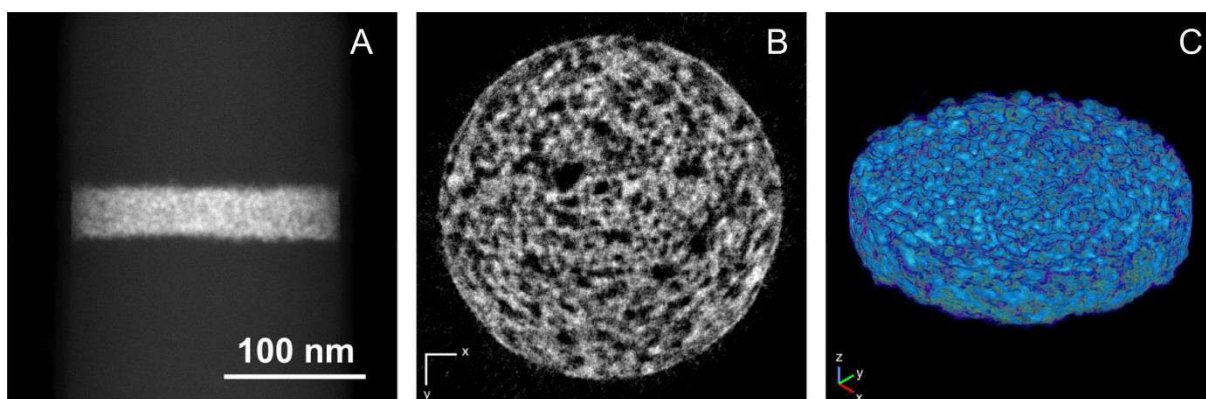
Figure 6: (A) HAADF-STEM projection image of the ZnO/organic interfaces for the annealed tandem cell (2 min at 70° C). (B) An orthoslice through the 3D reconstruction of the ZnO layer in the micropillar specimen shows the porosity of the ZnO layer. (C): Volume rendering image from the 3D reconstruction of the ZnO layer.

In section 3.4 we show how quantitative electron tomography is used as a tool to obtain quantitative information of the surface area at the interface between hard and soft materials in a single junction model (P3HT:PCBM) solar cell device.

3.2   Nanoscale morphology of photoactive layers

It is well known that the BHJ morphology at the nanoscale is crucial for device performance of organic solar cells. To visualize the material domains of different compositions we apply STEMSI using spatially resolved spectra of the low energy-loss region as explained in section 2.5. Examples of high-quality EEL spectra are shown in Figure 7 for the model materials P3HT and PCBM. The clear differences in optical excitation signals, such as bulk and π-plasmons, illustrate why it is possible to obtain chemical contrast using these variations. The third spectrum from an averaged area of a P3HT:PCBM blend lies between signals of pure materials.
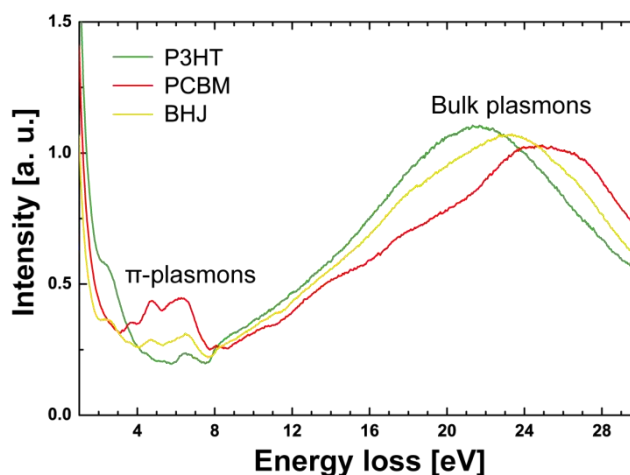
Figure 7: Low energy-loss spectra of P3HT, PCBM, and of a blend using both materials in a 1:1 mass ratio. The comparison shows that optical excitations are specific for the polymer and fullerene derivative, with the blend spectrum lying between signals of pure materials. The observed variations can be used to separate material domains in blends using similar, spatially resolved spectra.

For deciphering structures of full devices within the consortium, before STEMSI investigations cross-sections need to be prepared to obtain views of the stack architecture. One example is shown in
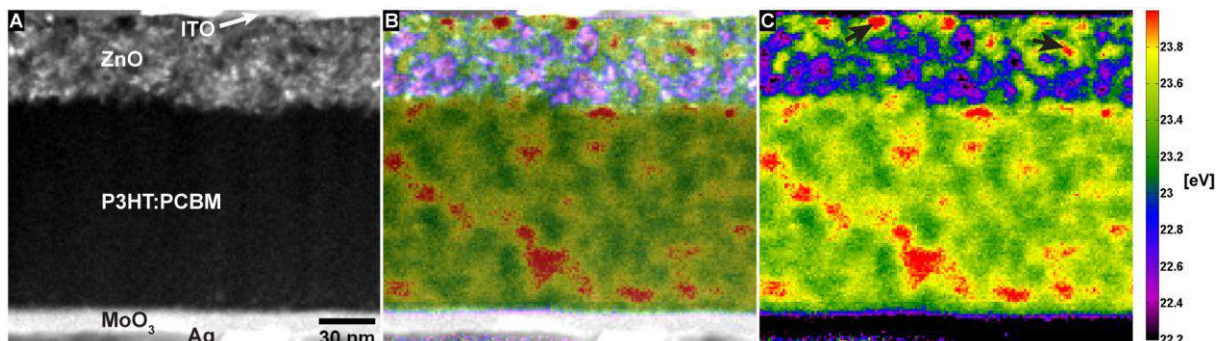
Figure 8. The device was received from UJI (Antonio Guerrero). It contains an inverted structure of ITO/ZnO/P3HT:PCBM/MoO$_3$/Ag. The photoactive layer was prepared using chloroform as solvent. The dark field image in
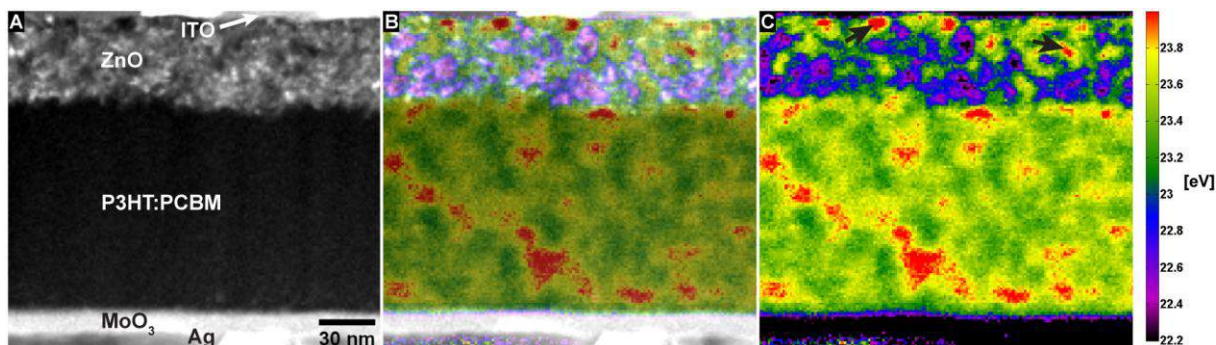
Figure 8A shows contrast to discriminate the various inorganic layers and interfaces to the photoactive layer. Therefore while scanning across the selected area, low-loss EELS spectra were recorded for each scan position. After correction (e.g. removal of background) bulk plasmon peaks were fitted for each spectrum with a Gaussian. Subsequently, the energy of the peak position can be mapped out to create a map showing the morphology according to spatially varying differences in domain composition. For
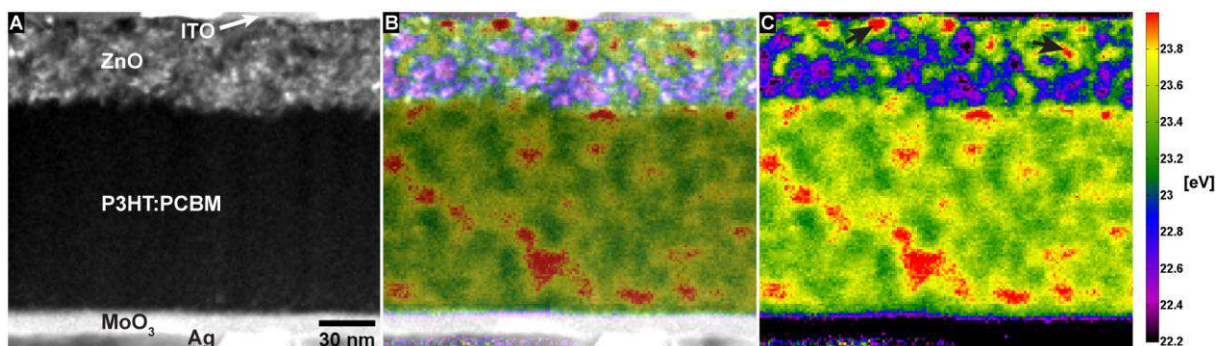
Figure 8B such a map in false-colour representation is overlaid with the dark-field image. Within the organic layer the domain distribution appears, with P3HT-rich domains in green, PCBM-rich in red and mixed areas in yellow. The map and the corresponding colour bar are presented in
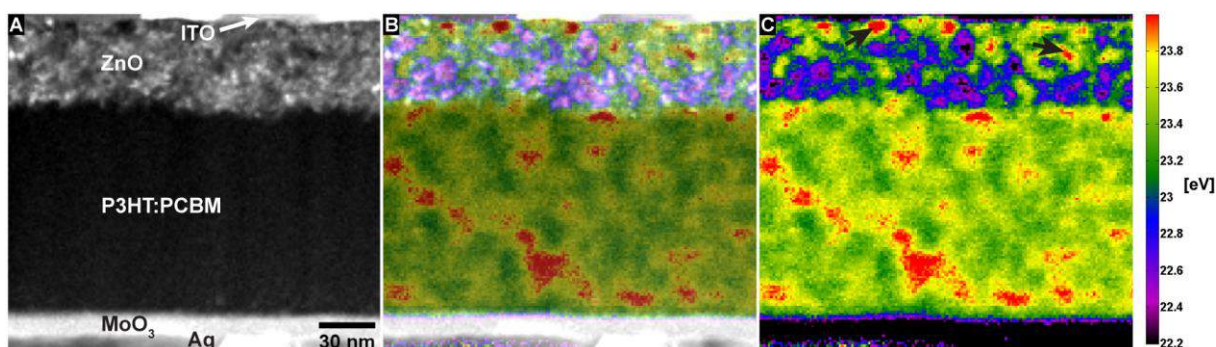
Figure 8C. It can be seen that enriched domains are distributed evenly throughout the layer, in lateral and vertical device directions, with large mixed areas in between. Another important result from
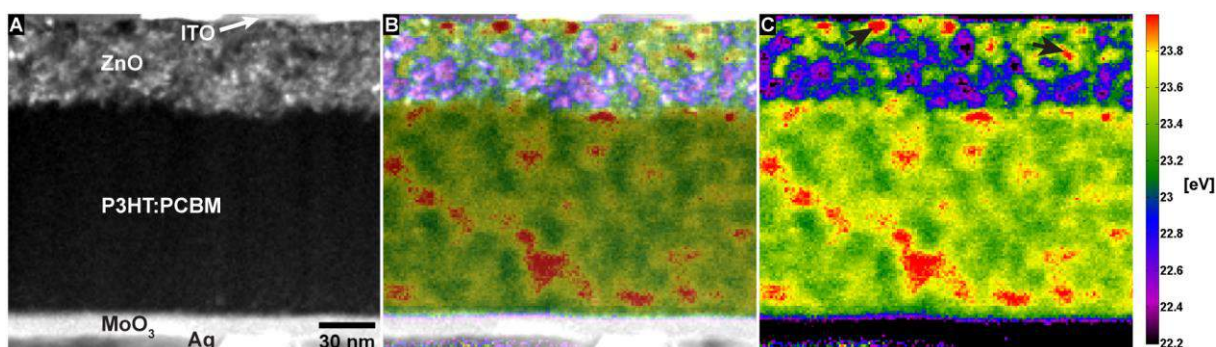
Figure 8 is that within the pores of the ZnO layer, PCBM enrichments are observed (see arrows for examples in
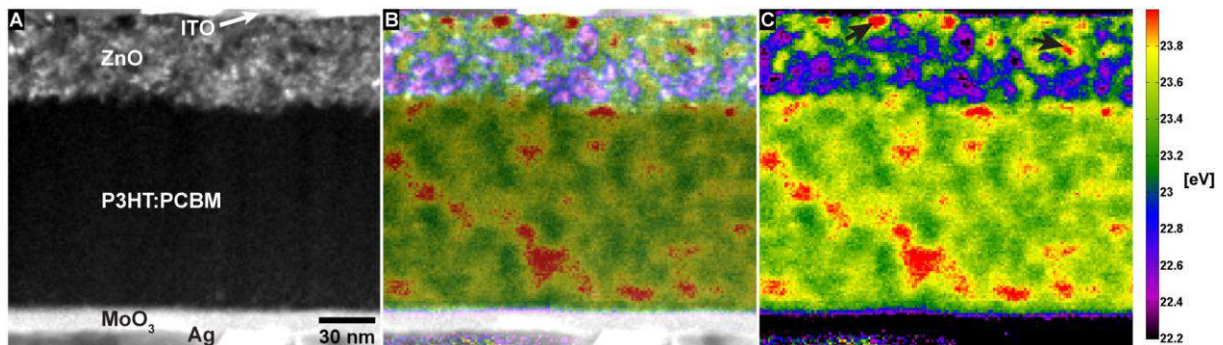
Figure 8C). This indicates that after depositing the solvated organic materials onto the ZnO mainly PCBM molecules can move into the pores increasing the interface between the electron transport material and cathode. This is not seen in dark field images of device cross sections.
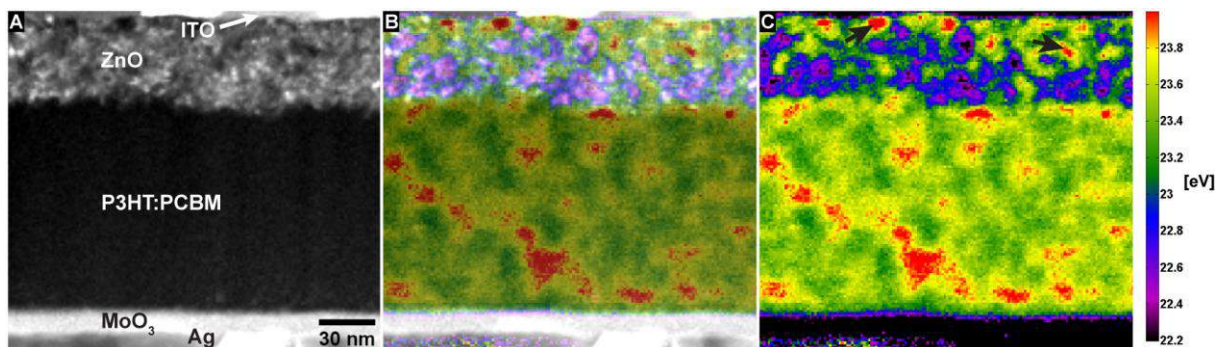
Figure 8: Dark field STEM and STEMSI analyses of a fresh device cross-section using P3HT:PCBM. Interfaces and layers comprising inorganic materials are seen in dark field mode (A). However, the overlay with the map of plasmon peak positions obtained from low energy-loss STEMSI data shows that the morphology of the photoactive layer can only be visualized using spectroscopic information (B). Sizes and distributions of material domains can be analysed using this plasmon peak map (C). Qualitative differences in compositions can be seen using the applied colour map.

3.3   Correlation of the morphology and processing parameters

By applying STEMSI to devices prepared using different processing conditions correlations between characteristic electrical properties and morphologies can be determined. As an example we provide results of an identical analysis in Figure 9A-C. Here the device was prepared like the device shown in
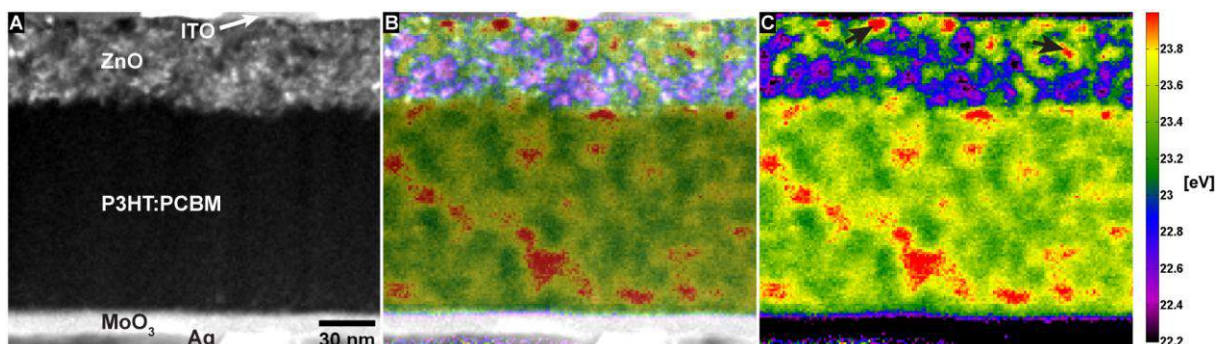
Figure 8. However, in this case it was stored for one year in the glove box to test whether storage for a longer time period changes the performance. As measured by the consortium partner, surprisingly the efficiency increased from 0.9 to 1.9 %. One explanation for this improvement over time is revealed by STEMSI. As seen in Figure 9B,C we observe a small increase of demixing accompanied by a slight decrease of the intermixed phase. These morphological properties have been shown to be beneficial for P3HT:PCBM solar cells [8]. Moreover, a PCBM layer formed at the ZnO hole blocking layer (black arrow in Figure 9C). So, electron transport and extraction is enhanced in comparison to the fresh device.
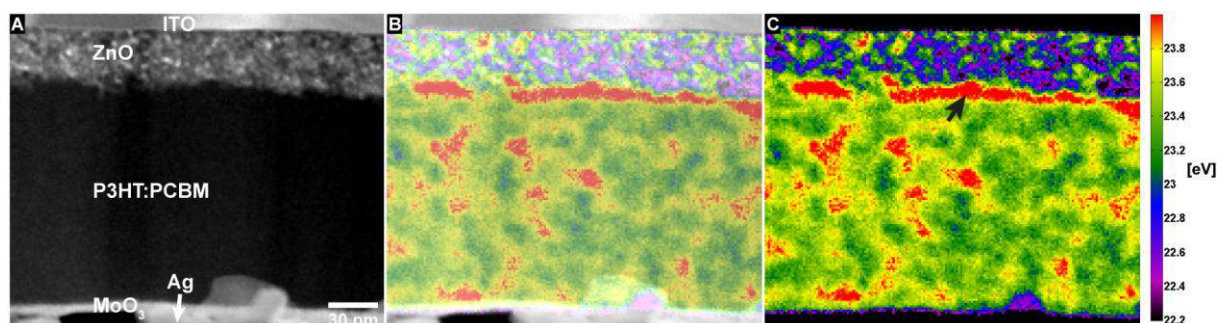
Figure 9: Dark field STEM and STEMSI analyses of a cross-section from an aged P3HT:PCBM device. As for the fresh device dark field contrast allows investigations of layers and interfaces containing inorganic materials (A) whereas the plasmon peak map (B,C) reveals the morphological properties of the organic materials. The arrow in (C) points to a PCBM layer that has formed at the cathode, which is particularly beneficial for the short-circuit current, hence, for the efficiency.

Another correlation of morphology and performance parameters is exemplified in Figure 10. Here, similar analyses to the chloroform devices were performed for devices prepared from orthodichlorobenzene (ODCB) as solvent. Figure 10A-C shows dark field and STEMSI results for a cross-section from a fresh device, Figure 10D-F for a device, which was also stored for one year. In the case of ODCB the power conversion efficiency was ~3% in the beginning as measured by the consortium partner and decreased to 1.3%. It cannot be explained from the morphology, why the fresh ODCB prepared sample shows a much higher efficiency than the sample prepared from chloroform. Here, results from other characterization methods must be incorporated. However, Figure 10 shows that after storage there is a large increase of the size of PCBM domains. As the colour map for Figure 10C and F are identical, it is obvious that PCBM forms several large domains. Although PCBM is still present in the bottom part of the photoactive layer, this leads to a strong decrease in polymer:fullerene interfacial area. This prevents efficient charge separation and can be determined as a reason why measured short-circuit current and fill factor decrease upon aging.
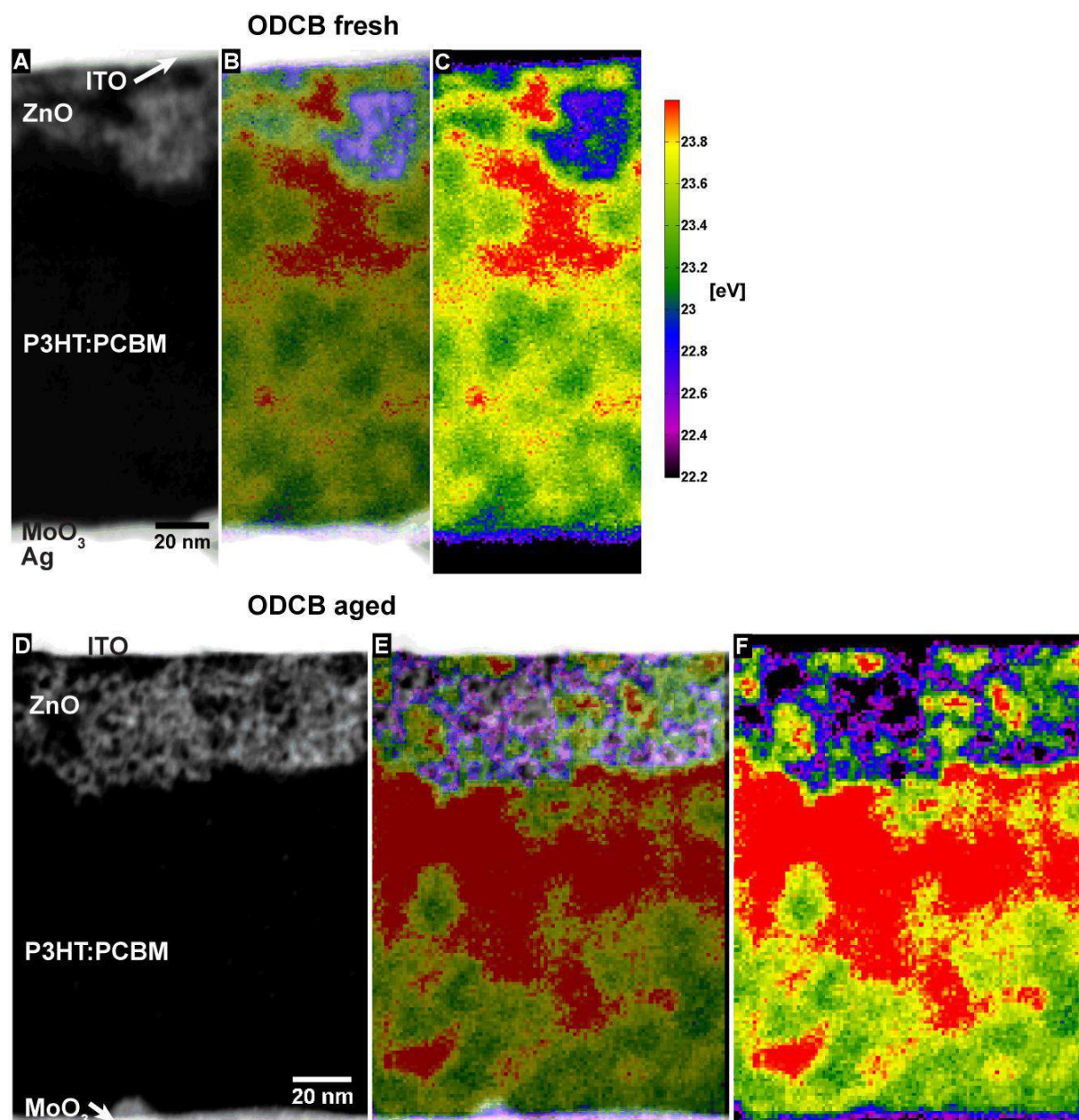
Figure 10: Dark field and STEMSI results for device cross-sections with blends casted from ODCB. The nanomorphology of the fresh photoactive layer (A-C) is similar to the layer casted from chloroform. However, the change after one year of aging is very pronounced (D-F). The layer of the aged ODCB sample shows very large PCBM domains, too large to form finely interspersed structures that are assumed to be required for organic BHJs.

3.3.1   Application to hero tandem cell

As the applicability of spectral mapping using STEMSI is successfully shown for model systems, we also use this method to visualize the morphology of the so far highest performing device within the consortium. The structure and morphology of all layers from a cross-section of a fresh device are shown in Figure 11. Again the organic layers' morphology becomes visible using high-resolution spectral imaging and appropriate data analysis. For both photoactive layers with high-performing polymers domain sizes are similar. However, with this 2D analysis the PDPP5T:PCBM blend appears to form less polymer enriched domains. At almost all organic-inorganic interfaces, the correct material is found. Only the interface between the PDPP5T:PCBM and the recombination layers shows an enrichment of the wrong material, which is in this case PCBM. Thus, here the morphology of the tandem cell can still be improved for better performance. The arrow in Figure 11 indicates the PEDOT:PSS layer from the recombination area. This material is seen as dark green to blue in the colour coded plasmon peak map since its plasmon peak energy is typically lower than that of the polymer used in photoactive layers. ZnO areas are seen as blue to purple.

It has been observed in the consortium that the performance of devices containing HBG-1 is dependent on the stack, and non-optimised stacks can be seen to decline in performance upon heating. Therefore we heated the fresh device for 2 min at 70° C within the glove box and performed the same STEMSI analysis. Results are presented in Figure 12. The morphological map reveals that the content of PCBM-rich domains at the recombination layer in the lower active layer decreases, which is detrimental for electron transport towards recombination with holes from the upper cell.
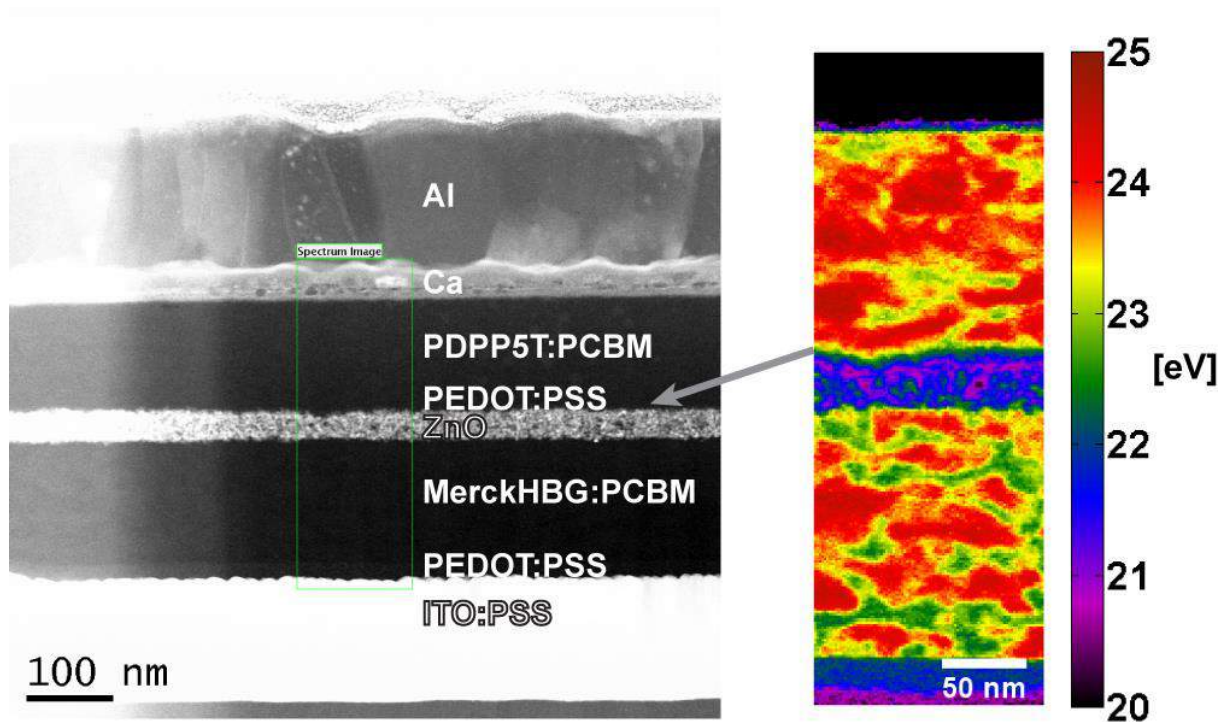
Figure 11: Structural and morphological analysis of a fresh high-performing tandem cell. The plasmon peak map on the right shows all layers that are also seen in the left dark field image and additionally the material domains within photoactive layers. PEDOT:PSS layers are shown in dark green to blue (grey arrow).
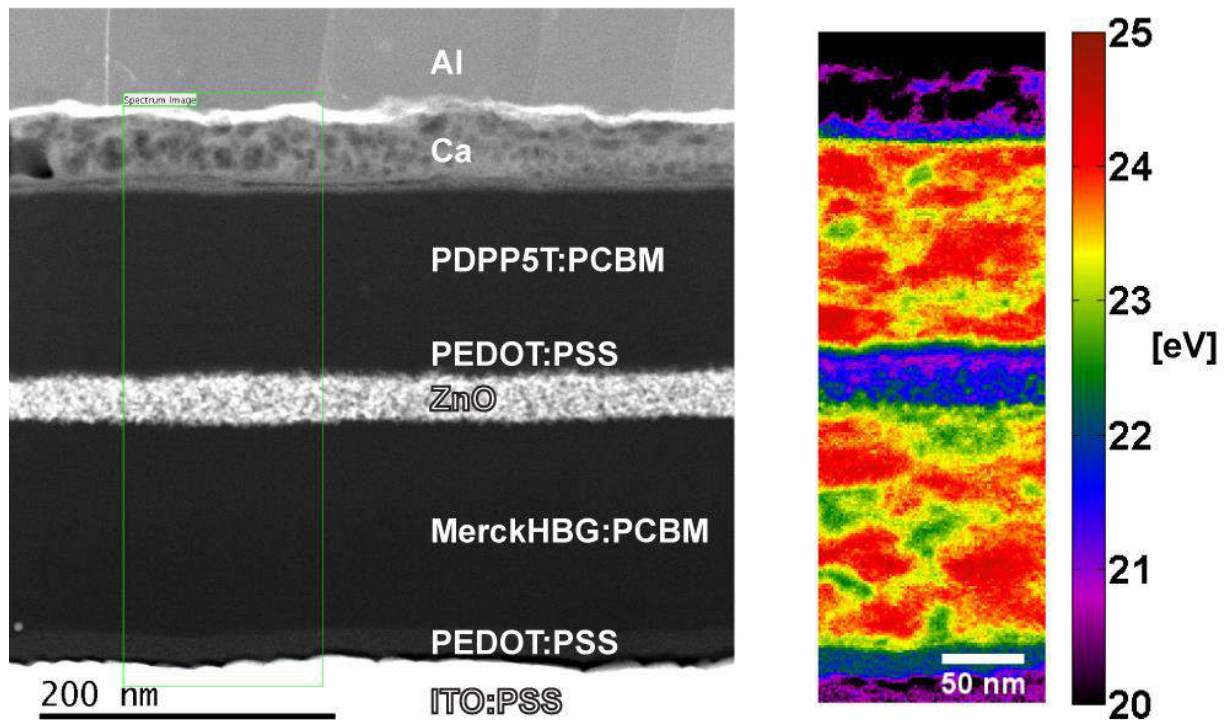
Figure 12: Structural and morphological analysis of a high-performing tandem cell that was heated for 2 min at 70° C in inert atmosphere. Photoactive layer morphologies are similar to the fresh device, however PCBM content is largely decreased at the recombination layer in the lower cell.

For a quantitative analysis of the lower cells of fresh and heated devices, power spectral densities (PSD) are computed from the plasmon peak maps. Such density spectra allow analysis of preferential occurrences of specific domain sizes within the photoactive layer [9]. Resulting densities shown in Figure 13 demonstrate that upon heating the peak that can be assigned to 35 nm for the fresh sample shifts to approximately 45 nm (black lines). This implies that heating induces growth of PCBM domains (as seen in the plasmon peak maps).
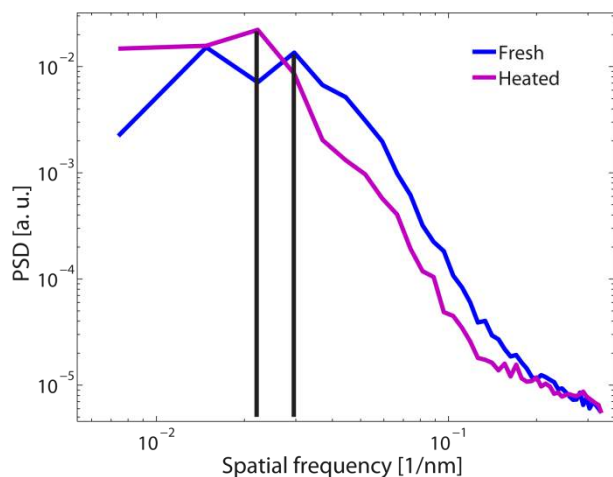
Figure 13: Power spectral densities from the lower cell plasmon peak maps of fresh and heated tandem cell devices. A peak at spatial frequencies corresponding to preferential domain sizes of 35 nm in the fresh cell shifts to 45 nm for the heated cell.

3.4   Quantitative electron tomography

As mentioned earlier in section 3.1 and 3.3, it is important to understand the correlation between the morphology of the interfaces and the electrical properties of the device. As case study we use the single junction model device where the organic blend is casted using ODCB as solvent. We have investigated the interface between the hole blocking layer ZnO and the organic blend. As mentioned earlier the two samples are a freshly prepared device and an aged device which was stored for one year in the glove box. Impedance spectroscopy measurements made by one of consortium partners (UJI) indicates that the efficiency of the aged device decreased in comparison to the fresh device (cf., section 3.3). For quantitative electron tomography experiments two pillar shaped specimens are prepared using FIB and mounted at the tip of an on-axis dedicated tomography holder to perform an acquisition over ±90°. Figure 14A indicates a HAADF-STEM projection of the micropillar specimen. The bright region at the bottom is ITO, on top of it there is an inhomogeneous layer of ZnO followed by the organic blend (PCBM:P3HT). Figure 14B shows an orthoslice through the 3D reconstruction of the ZnO/blend interfaces. A threshold based segmentation enabled to determine the interface area of the ZnO particles in 3D (Figure 14C). Earlier in 3.2 we showed that material from the organic blend penetrates into the porous layer of ZnO during deposition. Therefore the surface area of the porous ZnO layer can be an indication of the contact interface between ZnO and the photoactive layer. A comparison between the porous interface of the ZnO layer and cross-sectional area of the pillar shows that the surface area of the pores is approximately 7 times larger than the cross-section of the pillar.
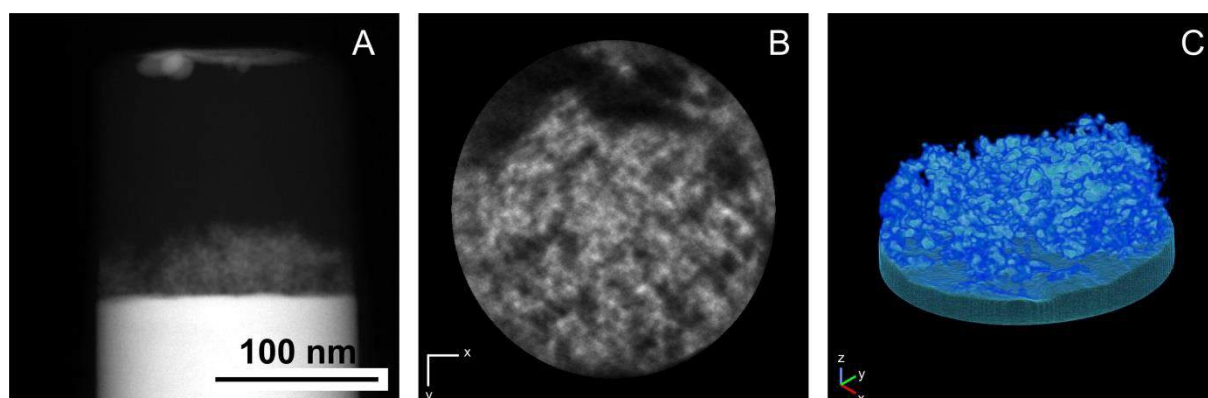
Figure 14: (A) HAADF-STEM projection image of the micropillar specimen prepared from the fresh P3HT:PCBM device casted from ODCB. The bright region at the bottom is ITO and on top the grey area is ZnO. (B) Orthoslice through the 3D reconstruction of the ZnO layer and a volume rendering representation of the ZnO layer only (C).

Figure 15A shows a similar projection image of the micropillar of the aged device. Figure 15B represents an orthoslice through the 3D reconstruction of the specimen and despite an inhomogeneity of the ZnO layer segmentation results show that the interface ratio between the ZnO/polymer blend interface and the cross-section of the pillar is 5. These ratios for both devices were validated by complementary tests made by the consortium partner Antonio Guerrero (UJI) using impedance spectroscopy. This case study proves that quantitative electron tomography can indeed be successful to obtain quantitative information in 3D at nanometer scale of the nanostructure of the device.
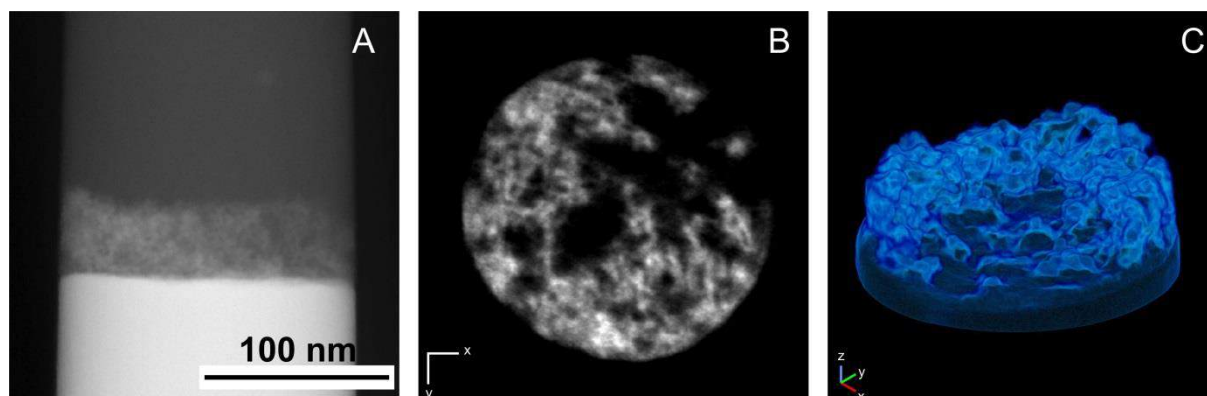
Figure 15: (A) HAADF-STEM projection image of the micropillar specimen prepared from the aged P3HT:PCBM device casted form ODCB. The bright region at the bottom is ITO and on top the grey area is ZnO. (B) Orthoslice through the 3D reconstruction of the ZnO layer and a volume rendering representation of the ZnO layer only (C).

3.5 3D morphology of photoactive layers by tomography of low energy-loss spectral images

It was shown that investigations of cross-sections provide detailed information about morphological parameters at the nanoscale. However, results are based on projections through sections of approximately 50 nm thickness. Therefore a needle or pillar-shaped sample of the heated high-performing tandem cell was prepared. As shown before, projections from all tilt angles up to 90° can be obtained. For the following investigation not only HAADF or dark field information is recorded for each tilt angle but also STEMSI data sets. An example dark field image with a corresponding image from an energy window where polymers show higher signal than fullerene domains is shown in Figure 16A,B.
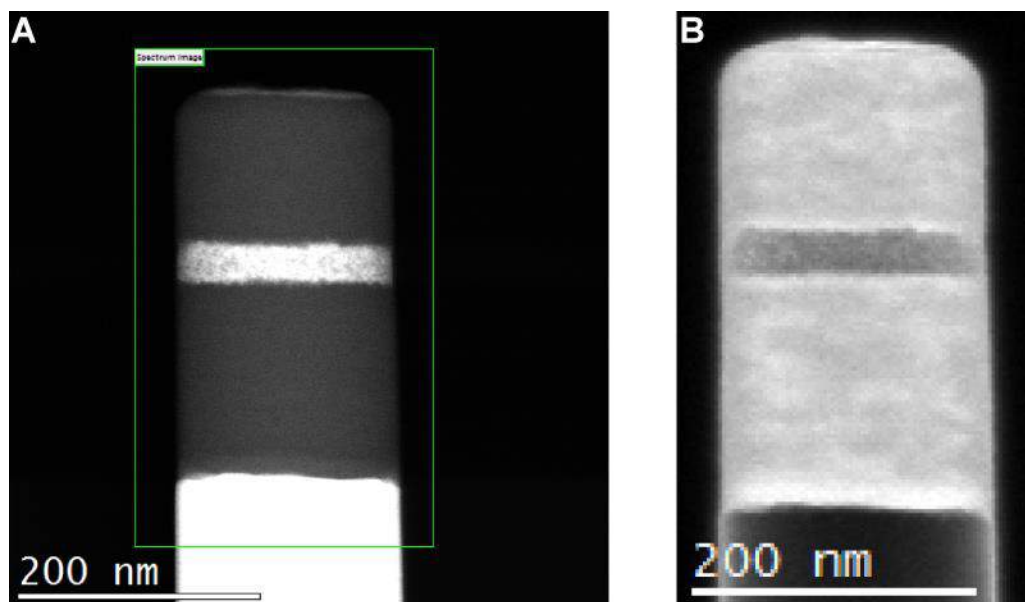
Figure 16: Exemplary dark field (A) and energy-loss image (B) from a pillar-shaped sample of the heated tandem cell. In sum 91 of these data sets were acquired for 91 tilt angles from -90 to 90° in steps of 2° to obtain a 3D reconstruction of low energy-loss spectra.

With a tilt angle increment of 2° this resulted in 91 spectra data sets, which were aligned and corrected for background signals. Reconstruction was done for all energy channels of the acquired spectra leading to a reconstruction of a four-dimensional data set, where each voxel can be assigned a reconstructed spectrum. Spectra from all voxels were fitted with a Gaussian to determine the plasmon peak position. As seen before for 2D analyses these

energy values can be mapped out. However, now mapping in all three spatial dimensions is possible, which allows investigation of the 3D structure without overlay artefacts from projections through different domains. An orthoslice from the 3D plasmon peak map is shown in Figure 17. The voxel size is 2.6 nm, which means that the resolution is expected to be about 5 nm. All layers as well as different organic material domains are visible within this orthoslice.
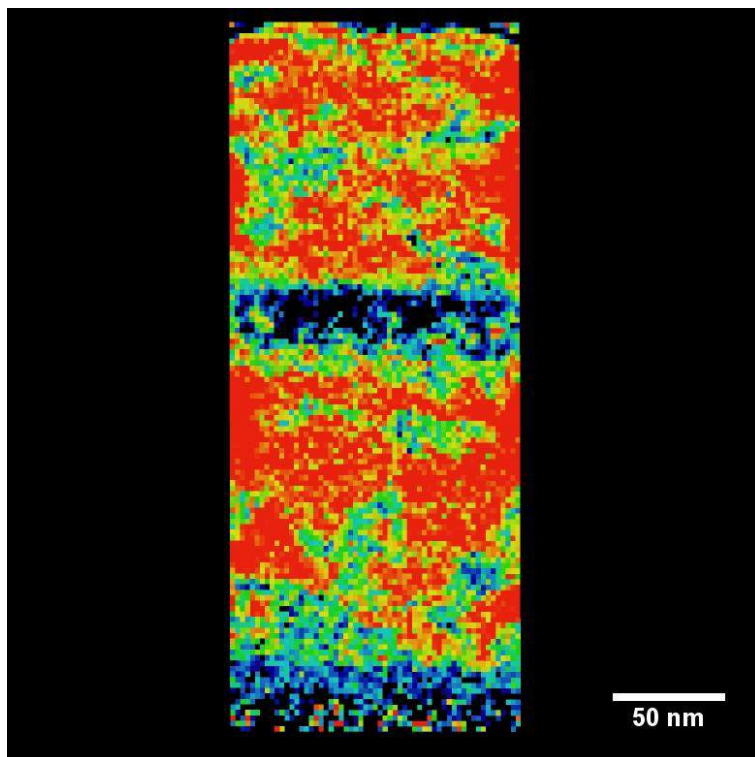

Figure 17: Orthoslice through the 3D map of fitted plasmon peak positions with a voxel size of 2.6 nm.
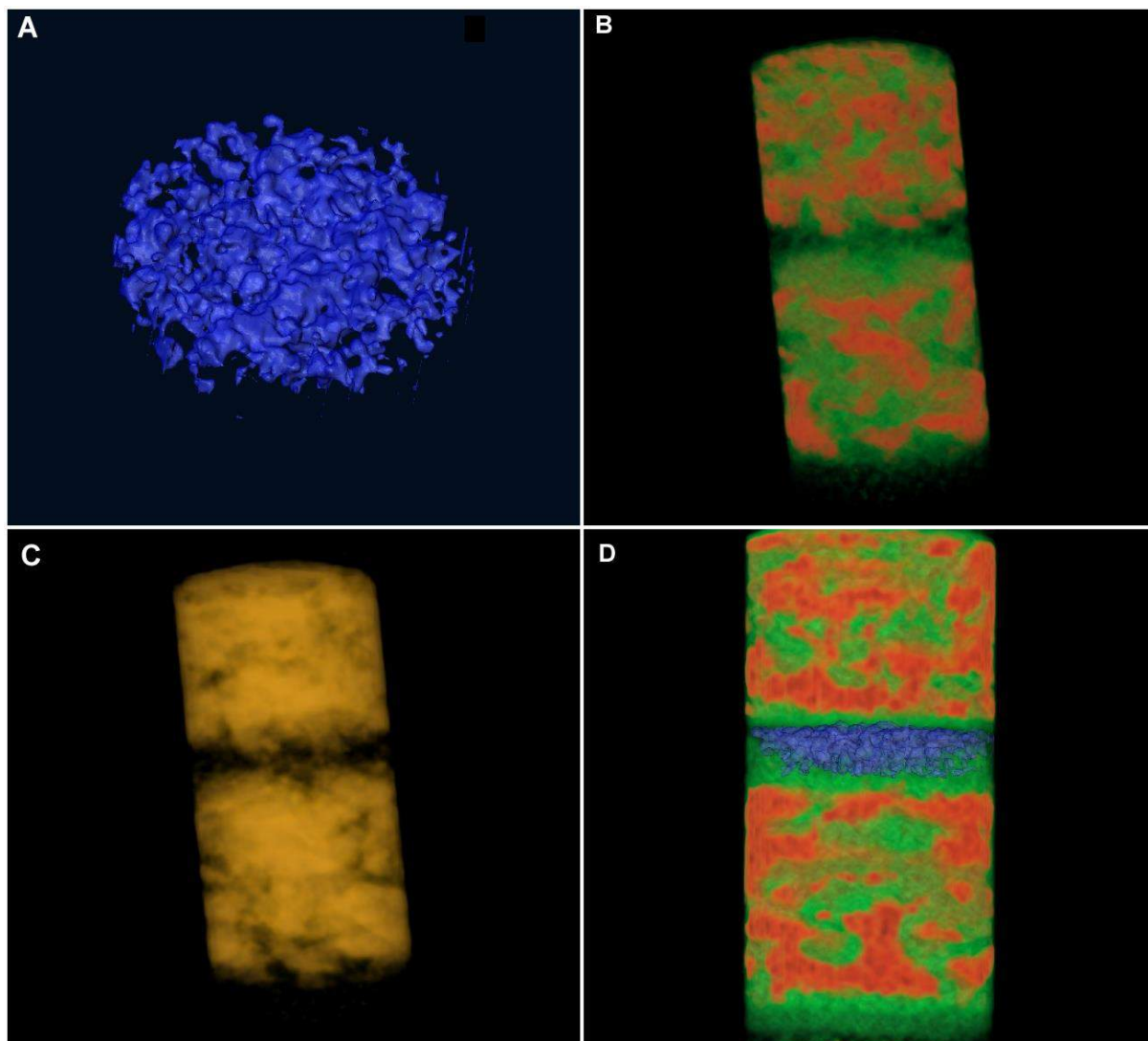
Figure 18: 3D renderings of the segmented ZnO layer (A), of enriched polymer and PCBM domains (B) and of the intermixed phase (C) as segmented from intermediate plasmon peak positions. A combination of ZnO rendering with enriched domains (D) is shown to illustrate the analytic capabilities for deciphering organic-inorganic interactions.

Figure 18A shows the recombination ZnO layer, segmented by thresholding. The pore structure is clearly visible, which is not possible using maps from 2D projection data. In Figure 18B a 3D rendering of polymer and PCBM-enriched domains is presented. It can be seen that PCBM-enriched domains of the upper cell that appear very large in 2D analyses are distributed throughout the layer. The rendering in Figure 18C shows the distribution of mixed phases, which are also segmented by thresholding of the energy values. A combination of the segmented ZnO layer and the enriched organic domains confirms that the PCBM content near ZnO in the lower cell is very low for the heated device. This can also be observed in Figure 19, where the segmented ZnO is shown with two orthogonal slices from the centre of the 3D map. It reveals examples of enriched and mixed phases from the inside of the cell as well as the organization of the recombination layer. PEDOT:PSS separates the photoactive materials of the upper cell from ZnO filling pores from the top. Holes from the bottom are filled by material from the lower cell with small PCBM content. Note that for Figure 18 and Figure 19 the reconstructed data was interpolated by a factor of two. This does, of course, not increase the inherent resolution but aids in interpretation of 3D rendered data.
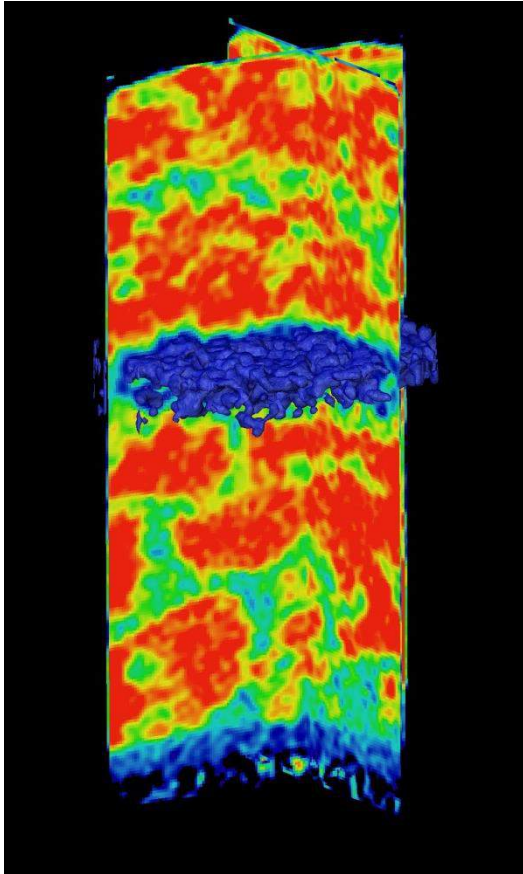
Figure 19: Segmented ZnO layer with two orthogonal slices allow a view into the inside of the device with its morphological properties of the photoactive layers as well as for transitional areas containing PEDOT:PSS and ZnO.

4 Conclusions

It was shown that HAADF-STEM imaging and tomography enables visualization of various device interfaces between soft and hard materials. As an example quantitative electron tomography provides 3D reconstruction and analysis of interfaces comprising ZnO layers, which are important as hole blocking layers in single junction cells or within recombination layers in tandem cells. The reconstruction of the porous ZnO structure at sub-nm resolution was used to determine the maximal interfacial area between ZnO and the applied organic materials. This supports the understanding of electronic processes, e.g., at cathodes of single junction cells.

Nanoscale morphology of photoactive layers was visualized in 2D using novel methods for data analysis of spatially resolved spectroscopic data on FIB prepared samples. This method was applied to devices using the model system P3HT:PCBM as well as to the high-performing tandem cell device architecture. Correlations to different fabrication conditions and treatments of devices reveal crucial reorganization processes within photoactive layers. For the first time it was demonstrated that spectral mapping is also possible in 3D using reconstructed low energy-loss data. The 3D morphology of a pillar-shaped sample of the tandem cell was visualized with a resolution of approximately 5 nm without reconstruction artefacts from conventional tomography on layer samples. This allows detailed analyses of the 3D morphological organization of all layers between the electrodes. In the future spectral segmentation in 3D can be used to obtain quantitative size and compositional information about material domains that largely determine the performance of organic solar cells.

5   References

[1]   Midgley, P. A. and Bals, S. (2012) Electron Tomography, in Handbook of Nanoscopy, Volume 1&2 (eds G. Van Tendeloo, D. Van Dyck and S. J. Pennycook), Wiley-VCH Verlag GmbH & Co. KGaA, Weinheim, Germany.

[2]   Heidari, H., Van den Broek, W. and Bals, S. A practical method to determine the effective resolution in incoherent experimental electron tomography, Ultramicroscopy 111, 330-336 (2011)

[3]   Hawkes, P. W. Electron Tomography: Three-dimensional Imaging with the transmission Electron Microscope. Frank, J. (ed.) (Plenum Press, New York; London,1992).

[4]   Goris, B., Bals, S., Van den Broek, W., Verbeeck, J, and Van Tendeloo, G. Exploring different inelastic projection mechanisms for electron tomography. Ultramicroscopy 111, 1262–1267 (2011)

[5]   Pfannmöller, M., Kowalsky, W. & Schröder, R. R. Visualizing physical, electronic, and optical properties of organic photovoltaic cells. Energy Environ. Sci. 6, 2871–2891 (2013).

[6]   Pfannmöller, M. et al. Visualizing a Homogeneous Blend in Bulk Heterojunction Polymer Solar Cells by Analytical Electron Microscopy. Nano Lett. 11, 3099–3107 (2011).

[7]   Egerton, R. F. & Takeuchi, M. Radiation damage to fullerite (C[sub 60]) in the transmission electron microscope. Appl. Phys. Lett. 75, 1884–1886 (1999).

[8]   Collins, B. A., Tumbleston, J. R., Ade, H. Miscibility, Crystallinity, and Phase Development in P3HT/PCBM Solar Cells: Toward an Enlightened Understanding of Device Morphology and Stability. J Phys. Chem. Lett. 2, 3135-3145 (2011).

[9]   Nisato, G., Ermi, B. D., Douglas, J. F., Karim, A. Excitation of Surface Deformation Modes of a Phase-Separating Polymer Blend on a Patterned Substrate. Macromolecules 32, 2356-2364 (1999).